Ultra-low diffusion barrier tetramethyl ammonium cation-intercalated layered MnO_2 for high-performance aqueous zinc-ion batteries

Zixiang Zhou, Jianbo Tong*, Xiaoliang Zou, Yue Wang, Yuxuan Bai, Yifan Yang, Youyong Li, Chao Wang*, Shuling Liu*

Department of Chemistry and Chemical Engineering, Shaanxi Collaborative Innovation Center of Industrial Auxiliary Chemistry & Technology, Key Laboratory of Auxiliary Chemistry and Technology for Chemical Industry, Ministry of Education, Shaanxi University of Science and Technology, Xi'an, Shaanxi 710021, China

*Corresponding author.

E-mail address: liushuling@sust.edu.cn

jianbotong@aliyun.com

cwang@sust.edu.cn

Experimental

Chemicals

The following reagents were used without further purifications. manganese chloride tetrahydrate ($MnCl_2·4H_2O$, AR, 99.0%), tetramethylammonium hydroxide pentahydrate ($C_4H_{13}NO·5H_2O$, AR, 97.0%), hydrogen peroxide (H_2O_2, AR, 30%), manganese sulfate tetrahydrate ($MnSO_4·4H_2O$, AR, 98.0%), zinc sulfate heptahydrate ($ZnSO_4·7H_2O$, AR, 98.0%), potassium chloride (KCl, AR, 99%), sodium chloride (NaCl, AR, 98%), magnesium chloride ($MgCl_2$, AR, 98%), calcium chloride ($CaCl_2$, AR, 98%), cobalt chloride hexahydrate ($CoCl_2·6H_2O$, AR, 98%), nickel chloride hexahydrate ($NiCl_2·6H_2O$, AR, 98%), and doubly distilled water.

Preparation of X-MnO_2 (X=Na, Mg, K, Ca, Co, Ni, Zn)

The preparation of X-MnO_2 (X = Na, Mg, K, Ca, Co, Ni, Zn) was similar to that of TMA-MnO_2. After washing, the MnO_2 were added to 1 M solutions of KCl, NaCl, $MgCl_2$, $CaCl_2$, $CoCl_2$, $NiCl_2$, or $ZnSO_4$. After allowing the mixture to stand at room temperature for 3 days, the suspension underwent centrifugation to gather precipitates, which were subsequently washed at least six times with deionized water. The final samples, labeled as Na-MnO_2, K-MnO_2, Ca-MnO_2, Mg-MnO_2, Co-MnO_2, Ni-MnO_2 and Zn-MnO_2, were obtained by freeze-drying the precipitates.

Material characterizations

Crystallographic phases of the samples were assessed using X-ray diffraction (XRD) employing a Bruker D8 Advance instrument in Bragg-Brentano geometry with a Cu target (λ = 0.154 nm). Thermogravimetric analysis (TGA) was conducted to analyze

the degradation pattern of precursor samples (post-drying) from room temperature to 600 °C at a heating rate of 5 °C min^{-1} under N_2 flow, utilizing a thermogravimetric analyzer (STA7200RV, Hitachi). X-ray photoelectron spectroscopy (XPS) measurements were performed using an AXIS SUPRA instrument (Renishaw-invia). Fourier transform infrared (FTIR) spectroscopy was executed using an INVENIO instrument (Bruker) to determine infrared spectra. Field emission scanning electron microscopy (FE-SEM) at an accelerating voltage of 10 kV equipped with energy-dispersive X-ray spectroscopy (EDS) (Xplore-30, Oxford) was employed to observe sample morphologies. Raman spectroscopy measurements were conducted using a Renishaw Invia Raman spectroscope. Transmission electron microscopy (TEM), High-resolution transmission electron microscopy (HR-TEM), and selected area electron diffraction (SAED) patterns were obtained utilizing the FEI Tecnai G2 F20 instrument with an acceleration voltage of 200 kV.

Electrochemical characterizations

The cathode of the ZIBs was fabricated using active material, acetylene black as the conductive agent, and polyvinylidene fluoride as the binder (with a weight ratio of 7:2:1), and N-methyl-2-pyrrolidone was utilized as the solvent during the process of ink slurry preparation. After continuous stirring, the resulting slurry was coated onto a stainless steel circular mesh with a diameter of 12 mm, followed by drying in a vacuum oven at 80 ℃ for 12 h. The active material loading was approximately 2 mg cm^{-2}. The electrochemical analysis of all samples was performed using a CR2032 coin cell with zinc foil as the negative electrode, glass fiber as the separator, and 2 M $ZnSO_4$ + 0.2 M

$MnSO_4$ aqueous solution as the electrolyte. Cyclic voltammetry (CV) and electrochemical impedance spectroscopy (EIS) were conducted using CHI660E or PARSTAT MC potentiostats. Unless specified otherwise, all potentials are referenced to Zn/Zn^{2+}. The CV scans were performed within the range of 1-1.85 V at a scan rate of 0.1 mV s^{-1}, while EIS measurements were carried out across a frequency spectrum from 10^5 to 0.01 Hz, with an alternating potential amplitude of 5 mV. A battery test system (LAND MTI-5 V 10 mA) was utilized to assess the cycling and charge–discharge characteristics of the coin cells. The galvanostatic intermittent titration technique (GITT) involved a series of galvanostatic discharge pulses (10 minutes at 100 mA g^{-1} followed by a 30-minute rest) within the potential range of 1-1.85 V. In situ electrochemical quartz crystal microbalance (EQCM, QCM922, Princeton) measurements combined with cyclic voltammetry and charge-discharge curves were used to explore the charge storage mechanism. Electrochemical tests were performed in a two-electrode cell configuration with TMA-MnO_2 coated on Au as the working electrode (prepared in the same process as the cathode) and Zn as the counter/reference electrode. EQCM data were analyzed based on the Sauerbrey equation:

$$\Delta_{mass} = \frac{-\Delta_{freq} * A * sqrt(uq * pq)}{2(Fq^2)}$$

Where Δ_{mass} is the mass change, Δ_{freq} is the resonance frequency change, A is the gold electrode surface (0.198 cm^{-2}), uq is the AT-cut quartz constant ($2.947x10^{-11}$ g cm^{-2}), pq is the quartz crystal density (2.65 g cm^{-2}), Fq is the reference frequency (9.00 MHz) All the electrochemical tests were performed at room temperature.

Density functional theory calculations

Calculations are conducted within the density functional theory (DFT) framework, employing the projected enhanced wave method and implemented using the Vienna Ab initio Simulation Package (VASP). Generalized gradient approximation (GGA) with Perdew-Burke-Ernzerhof (PBE) exchange functions is employed. The plane wave basis cutoff energy is set to 520 eV, and stringent convergence criteria are applied, with energy and force calculations requiring convergence to within 10^{-5} eV/atom and 0.05 eV/Å, respectively. For unit cell optimization of the MnO_2 and TMA-MnO_2 structures, a 2×1×1 Γ-centered grid is utilized as the Brillouin zone sampling scheme. In contrast, density of states calculations employ a 3×2×2 Γ-centered grid. The embedding structure of Zn undergoes optimization, with the original cell expanded and re-embedded using a 2×1×1 grid. The calculation of diffusion paths is carried out employing the Nudged-Elastic-Band (NEB) method. Additionally, for the optimization of the Zn embedding structure, a Γ-only Brillouin zone sampling scheme is employed.

Energy Density and Power Density

The energy density and power density were obtained by the following equations:

$$E = \int_0^{\Delta t} \frac{V \times i}{m} dt$$

$$P = \frac{E}{1000 \times \Delta t}$$

where E (Wh kg^{-1}) is the energy density, P is the power density (kW kg^{-1}), V (V), i (mA), m (g) and Δt (h) represent the working potential, discharging current, the mass loading of the cathode and the discharging time, respectively.

Diffusion Coefficient

The diffusion coefficient (D) is obtained from the following equation,

$$D = \frac{4L^2}{\pi\tau}\left(\frac{\Delta Es}{\Delta Et}\right)$$

where τ (s) is the constant current pulse time. The L is diffusion length (cm) of Zn^{2+} and H^+ which is equal to thickness of electrode. The ΔEs is the steady-state voltage change caused by the current pulse. The ΔEt are voltage changes during the constant current pulse.

Table S1.

Chemical components of the X-MnO_2 (X=Na, Mg, K, Ca, Co, Ni, Zn) with ICP-AES analysis.

Samples	**X: Mn Ratio (X=Na^+/Mg^{2+}/K^+/Ca^{2+}/Co^{2+}/Ni^{2+}/Zn^{2+})**
Na-MnO_2	0.43
Mg-MnO_2	0.16
K-MnO_2	0.23
Ca-MnO_2	0.29
Co-MnO_2	0.26
Ni-MnO_2	0.22
Zn-MnO_2	0.25

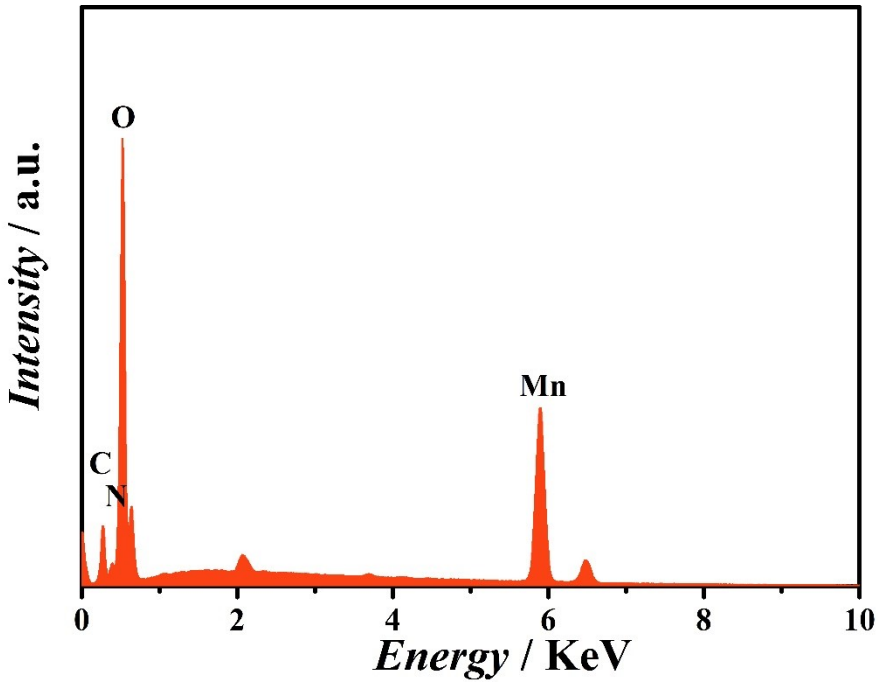

Fig. S1. EDS spectrum of TMA-MnO_2. The N/Mn ratio was estimated to be 0.14.

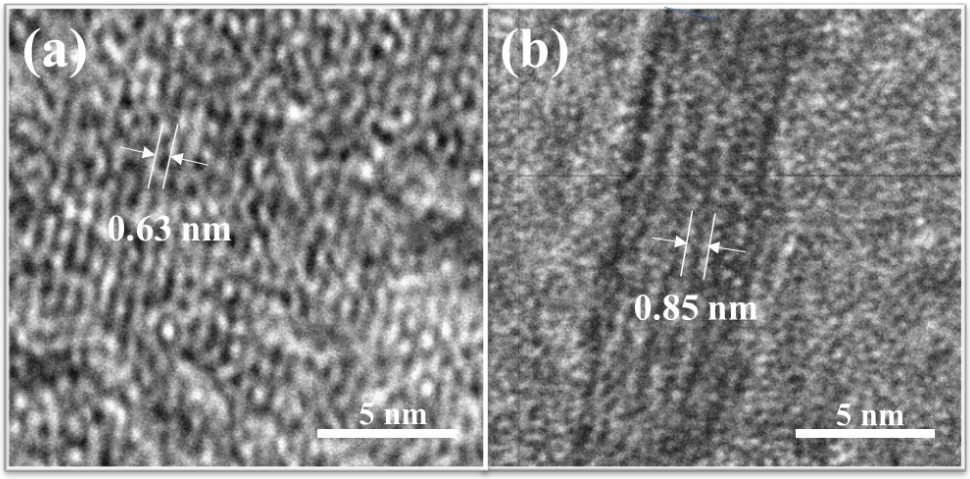

Fig. S2. HRTEM images of (a)MnO_2 and (b) TMA-MnO_2.

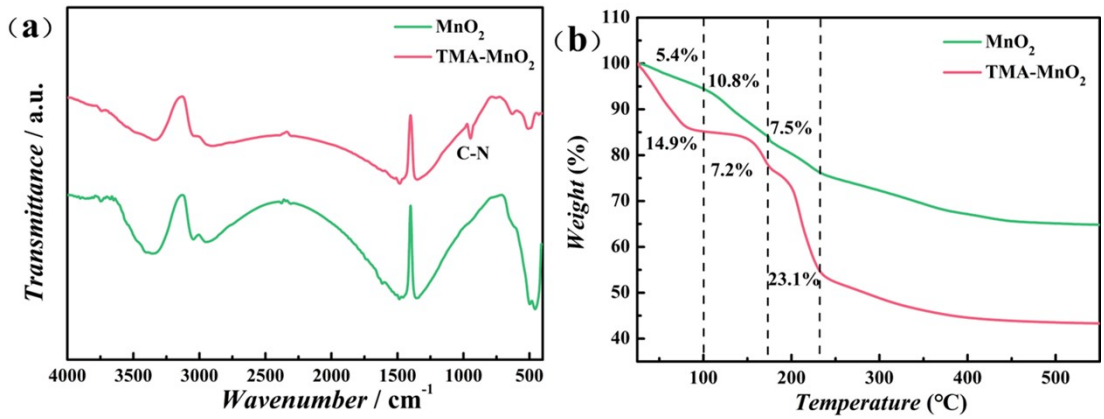

Fig. S3. (a) FTIR spectra and (b) TGA curves of the MnO_2 and TMA-MnO_2.

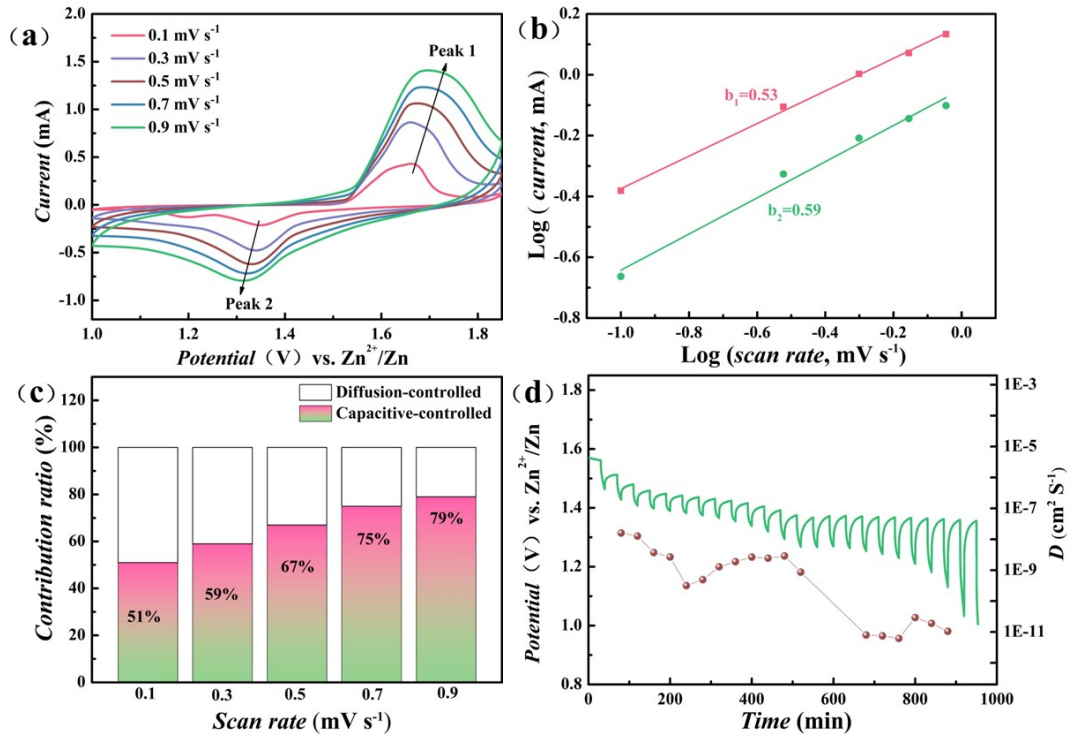

Fig. S4. (a) CV curve of the MnO_2 at 0.1 to 0.9 mV s^{-1}; (b) The relationship between log (peak current) and log (scan rate) plot of the MnO_2; (c) Capacitive-controlled process contribution to the capacity of the MnO_2; (c) GITT curve and the corresponding diffusivity coefficients in discharge process of the MnO_2.

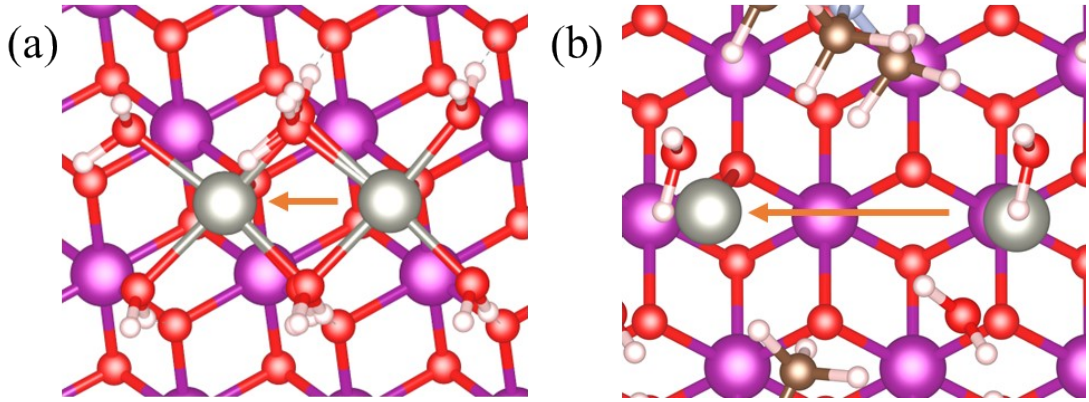

Fig. S5. Proposed diffusion path of the MnO_2 and TMA-MnO_2.

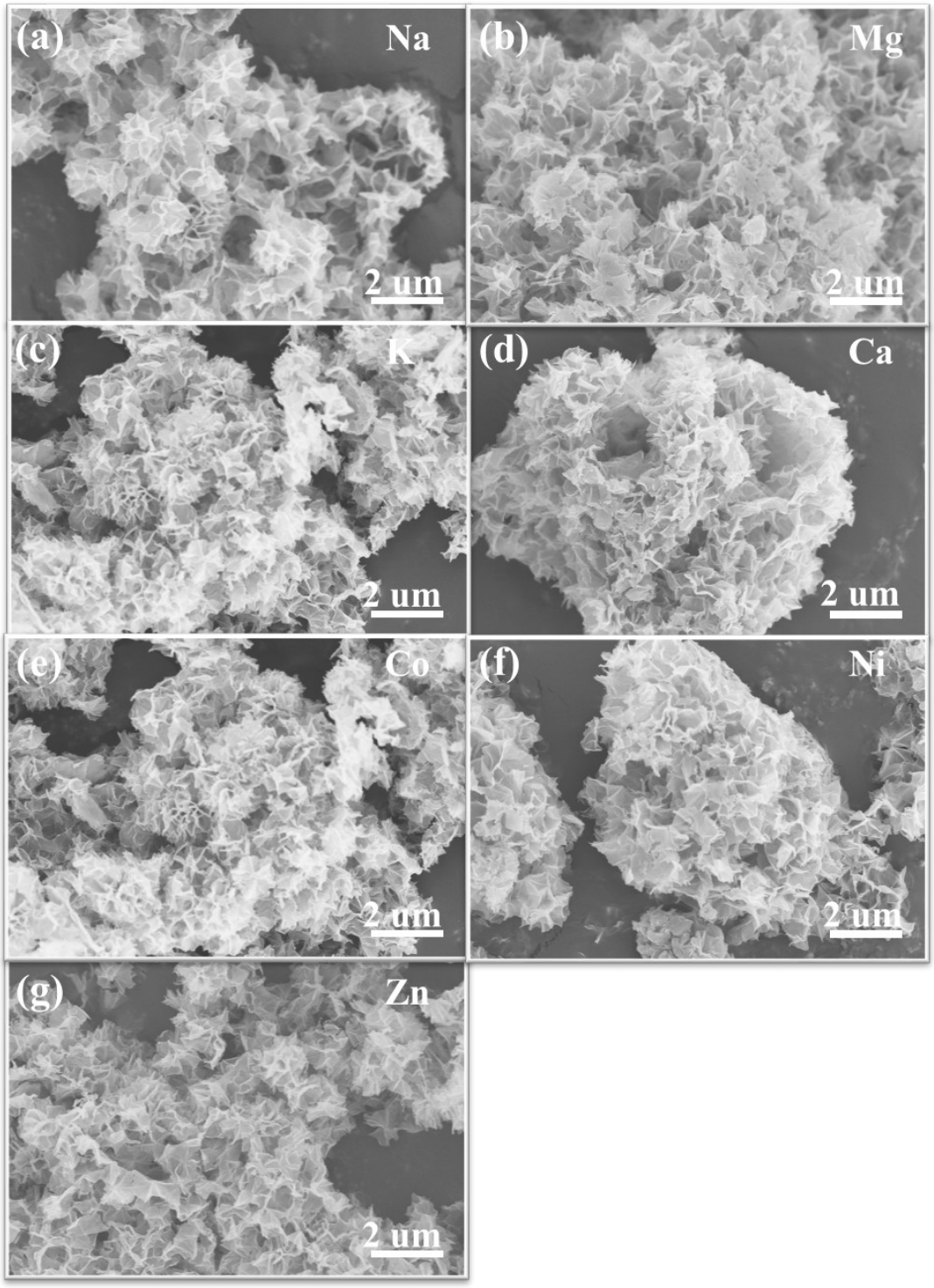

Fig. S6. SEM images of the X-MnO_2 (X=Na, Mg, K, Ca, Co, Ni, Zn).

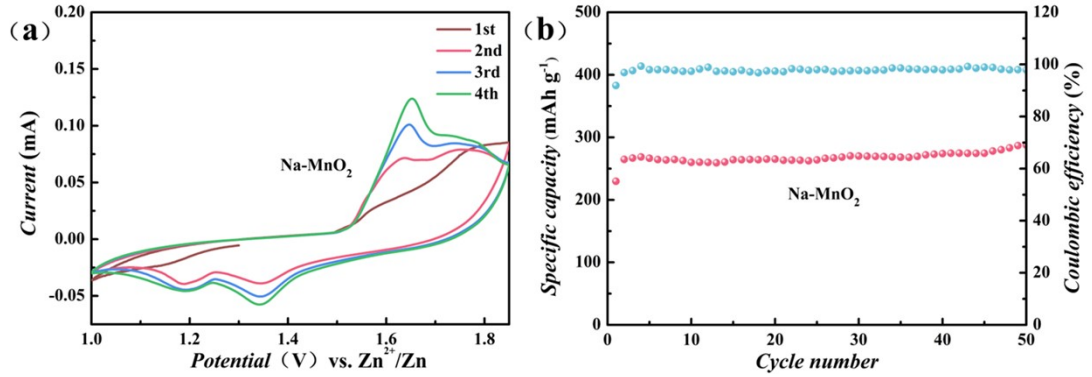

Fig. S7. CV of the Na-MnO_2 at the scan rate of 0.1 mV s^{-1}; (b) Long-cycle performance of Na-MnO_2 at 0.2 A g^{-1}.

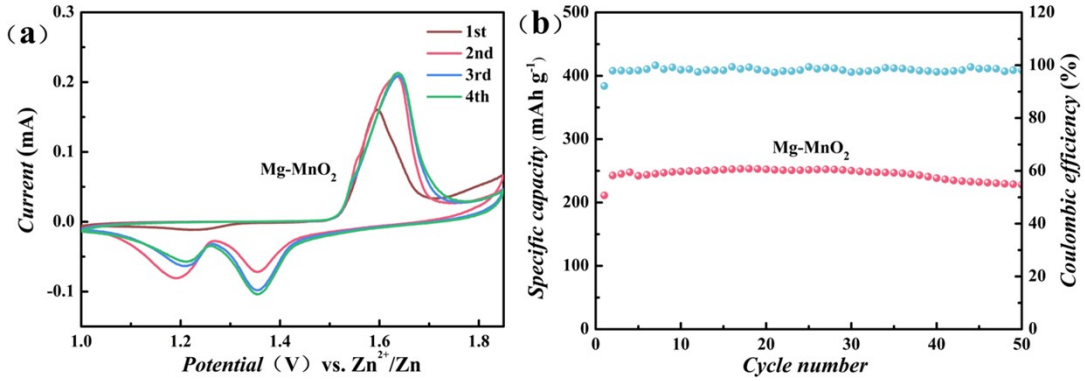

Fig. S8. CV of the Mg-MnO_2 at the scan rate of 0.1 mV s^{-1}; (b) Long-cycle performance of Mg-MnO_2 at 0.2 A g^{-1}.

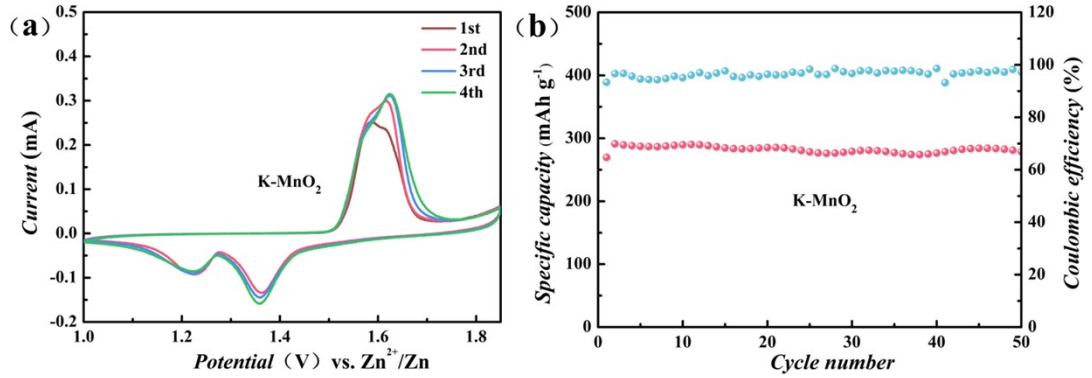

Fig. S9. CV of the K-MnO_2 at the scan rate of 0.1 mV s^{-1}; (b) Long-cycle performance of K-MnO_2 at 0.2 A g^{-1}.

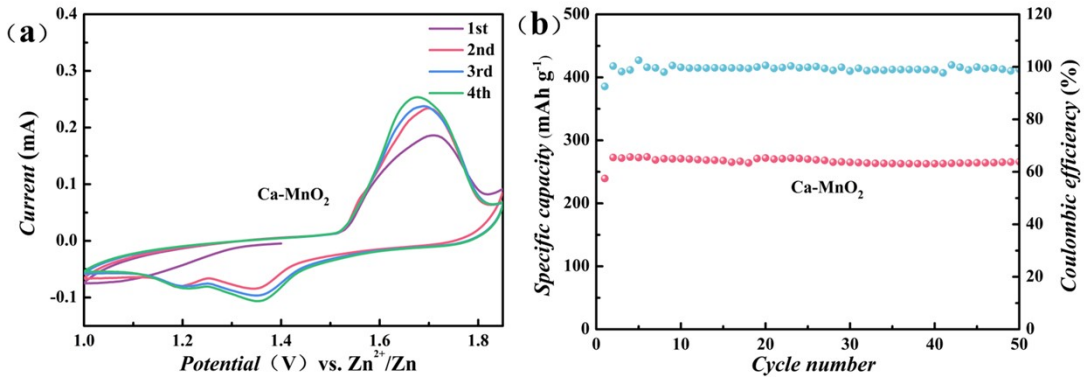

Fig. S10. CV of the Ca-MnO_2 at the scan rate of 0.1 mV s^{-1}; (b) Long-cycle performance of Ca-MnO_2 at 0.2 A g^{-1}.

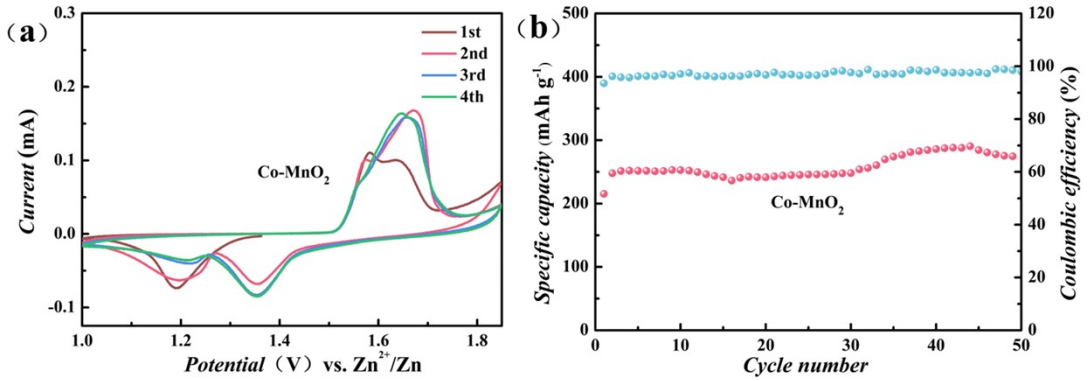

Fig. S11. CV of the Co-MnO_2 at the scan rate of 0.1 mV s^{-1}; (b) Long-cycle performance of Co-MnO_2 at 0.2 A g^{-1}.

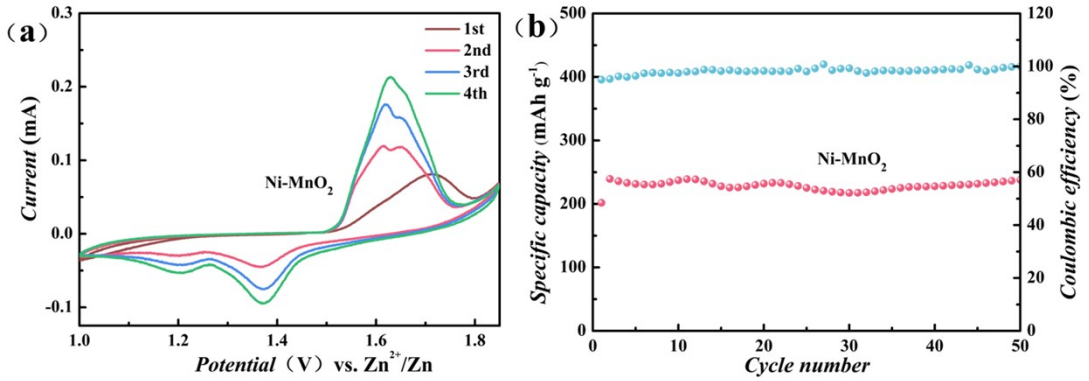

Fig. S12. CV of the Ni-MnO_2 at the scan rate of 0.1 mV s^{-1}; (b) Long-cycle performance of Ni-MnO_2 at 0.2 A g^{-1}.

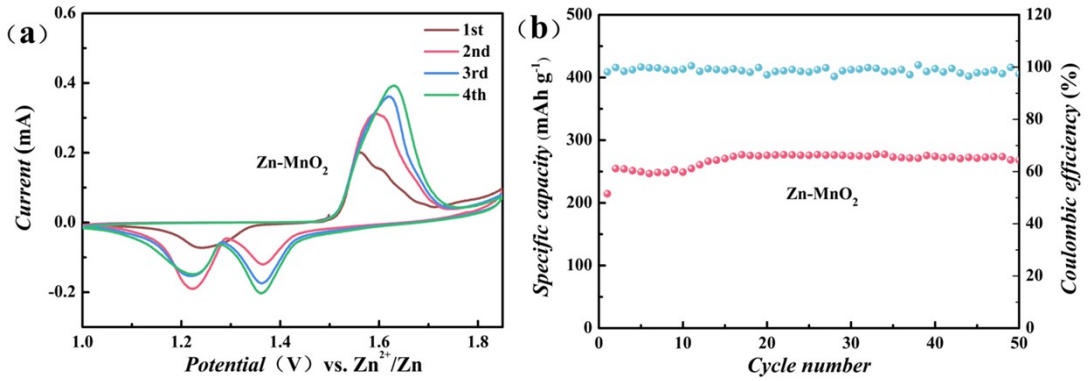

Fig. S13. CV of the Zn-MnO_2 at the scan rate of 0.1 mV s^{-1}; (b) Long-cycle performance of Zn-MnO_2 at 0.2 A g^{-1}.

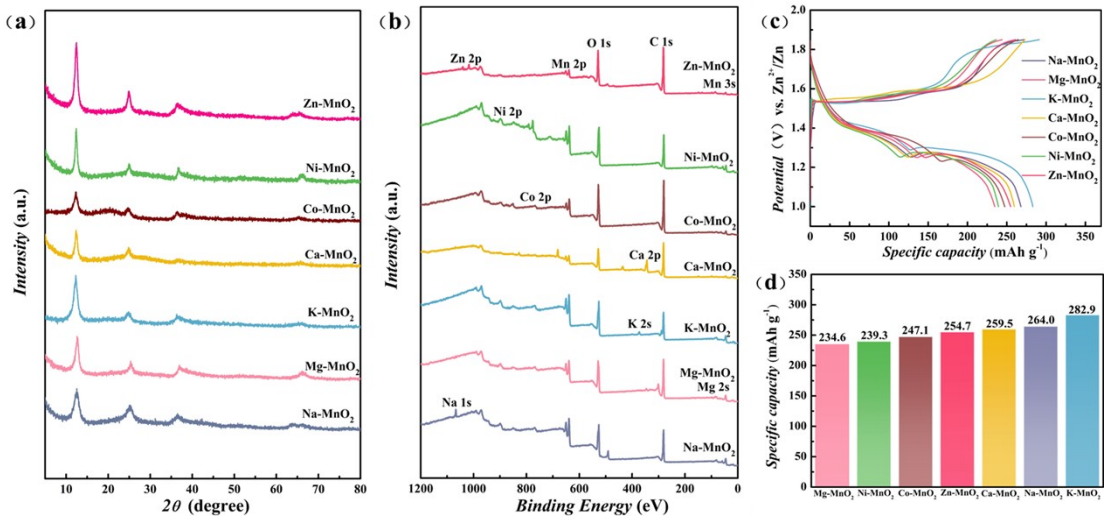

Fig. S14. (a) XRD patterns and (b) XPS survey spectra of the X-MnO_2 (X=Na, Mg, K, Ca, Co, Ni, Zn); (c) Charge and discharge curves of the X-MnO_2 (X=Na, Mg, K, Ca, Co, Ni, Zn) at 0.2 A g^{-1}; (d) Comparison of specific capacity of the X-MnO_2 (X=Na, Mg, K, Ca, Co, Ni, Zn).

To delve deeper into the electrochemical performance of various cation pre-intercalated MnO_2 as cathode materials for ZIBs, X-MnO_2 (where X=Na, Mg, K, Ca, Co, Ni, Zn) is synthesized using an ion exchange method. ICP-AES is used to determine the atomic ratio of X:Mn (X=Na, Mg, K, Ca, Co, Ni, Zn), MnO_2 pre-intercalated with different cations are finally denoted as $Na_{0.43}MnO_2$, $Mg_{0.16}MnO_2$, $K_{0.23}MnO_2$, $Ca_{0.29}MnO_2$, $Co_{0.26}MnO_2$, $Ni_{0.22}MnO_2$, and $Zn_{0.25}MnO_2$ (Table S1). Fig. 7a shows the XRD patterns of X-MnO_2. The presence of (001) and (002) crystal planes corresponding to the layered structure indicates that the crystal structure of MnO_2 is stable during the ion-exchange process. In addition, compared with TMA-MnO_2, the peak of (001) has a large shift to the right, indicating that in the high-concentration metal ion solution, TMA^+ is completely released, and the metal cations in the solution enter the interlayer, forming

X-MnO_2. It is worth noting that the (001) peak direction of X-MnO_2 after different ion exchange is shifted to different degrees, which may be related to the ionic radius. The larger the ionic radius, the smaller the rightward shift. The XPS survey spectra (Fig. 7b) of the X-MnO_2 shows the existence of Mn, O and X (X = Na, Mg, K, Ca, Co, Ni, Zn), which indicates the successful preparation of X-MnO_2. The SEM images in Fig. S6 display X-MnO_2 with a consistent nanosheet morphology across all samples, suggesting that TMA-MnO_2 underwent a re-self-assembly process subsequent to exfoliation in solution. To reveal the zinc ion storage capacity of X-MnO_2, we compare charge and discharge curves (Fig. 7c) of different ion-intercalated MnO_2 at 0.2 A g^{-1}. Consistent with other literature reports, X-MnO_2 exhibits a charge-discharge platform of H^+ and Zn^{2+}, and its specific capacity is intuitively shown in Figure 7d. The specific capacities of Na-MnO_2, Mg-MnO_2, K-MnO_2, Ca-MnO_2, Co-MnO_2, Ni-MnO_2 and Zn-MnO_2 are 264.0, 234.6, 282.9, 259.5, 247.1, 239.3 and 254.7 mA h g^{-1}, respectively. Fig. S7, 8, 9, 10, 11, 12 and 13 present the CV curves at 0.1 mV s^{-1} and the extended cycle performance at 0.2 A g^{-1} for Na-MnO_2, Mg-MnO_2, K-MnO_2, Ca-MnO_2, Co-MnO_2, Ni-MnO_2, and Zn-MnO_2, respectively. X-MnO_2 exhibits similar electrochemical behavior and have excellent cycling stability at 0.2 A g^{-1}. It is noteworthy that the capacity and stability of MnO_2 with various metal ion pre-intercalation layers is contingent not only upon ionic radius but also upon the relative abundance of metal ions incorporated within the MnO_2 lattice. In summary, this approach offers a novel method for investigating the zinc ion storage capabilities of various ion pre-intercalated MnO_2, enabling further exploration of diverse cation

effects on the charge storage mechanism in zinc ion batteries and expanding potential applications to other ion-based battery systems.

Table S2. Performance comparison of aqueous ZIBs with manganese oxide-based materials as cathodes.

Cathode material	Electrolyte	Specific capacity	Capacity retention	Ref.
TMA-MnO_2	2 M $ZnSO_4$+ 0.2 M $MnSO_4$	310.3 mA h g^{-1} at 0.2 A g^{-1}	91% after 1000 cycles at 2 A g^{-1}	This work
F-MO	2 M $ZnSO_4$+ 0.2 M $MnSO_4$	288 mA h g^{-1} at 0.1 A g^{-1}	96% after 200 cycles at 0.2 A g^{-1}	[1]
MnO_2 @MXene	2 M $ZnSO_4$+ 0.2 M $MnSO_4$	184 mA h g^{-1} at 0.05 A g^{-1}	84.5% after 1000 cycles at 0.1 A g^{-1}	[2]
HCM	2 M $ZnSO_4$+ 0.3 M $MnSO_4$	341 mA h g^{-1} at 0.2 A g^{-1}	87% after 3500 cycles at 2 A g^{-1}	[3]
ε- MnO_2@N	2 M $ZnSO_4$+ 0.5 M $MnSO_4$	183.4 mA h g^{-1} at 0.5 A g^{-1}	83% after 1000 cycles at 5 A g^{-1}	[4]
δ- MnO_2	1 M $ZnSO_4$	252 mA h g^{-1} at 0.083 A g^{-1}	43% after 100 cycles at 0.083 A g^{-1}	[5]
Mn_3O_4/CP	2 M $ZnSO_4$+ 0.2 M $MnSO_4$	201 mA h g^{-1} at 0.3 A g^{-1}	No decreasing after 200 cycles at 1 A g^{-1}	[6]
$ZnMn_2O_4$/NG	1 M $ZnSO_4$+ 0.05 M $MnSO_4$	232 mA h g^{-1} at 0.1 A g^{-1}	97.4% after 2500 cycles at 1 A g^{-1}	[7]
Ocu-Mn_2O_3	3 M $ZnSO_4$+ 0.1 M $MnSO_4$	241 mA h g^{-1} at 0.1 A g^{-1}	88% after 600 cycles at 1 A g^{-1}	[8]
δ-NMOH	2 M $ZnSO_4$+ 0.2 M $MnSO_4$	232 mA h g^{-1} at 2 C	Nearly 100% after 2000 cycles at 10 C	[9]
ZMO/CNTs	1 M $ZnSO_4$+ 0.1 M $MnSO_4$	220.3 mA h g^{-1} at 0.1 A g^{-1}	97.0% after 2000 cycles at 3 A g^{-1}	[10]
Mn_3O_4@HCFs	2 M ZnSO4+ 0.15 M MnSO4	215.8 mA h g^{-1} at 0.3 A g^{-1}	No decreasing after 1300 cycles at 0.4 A g^{-1}	[11]
Fe/α-MnO_2@PPy	2 M $ZnSO_4$+ 0.1 M $MnSO_4$	270 mA h g^{-1} at 0.1 A g^{-1}	71.4.% after 100 cycles at 0.1 A g^{-1}	[12]
α-MnO_2/CNT HMs	2 M $ZnSO_4$+ 0.1 M $MnSO_4$	296 mA h g^{-1} at 0.2 A g^{-1}	No decreasing after 100 cycles at 0.2 A g^{-1}	[13]
Ti-MnO_2	3 M $Zn(CF_3SO_3)_2$ + 0.1 M	259 mA h g^{-1} at	80% after 4000 cycles at	[14]

	$Mn(CF_3SO_3)_2$	0.1 A g^{-1}	1 A g^{-1}

References

1. D. Wang, Z. Liu, X.-W. Gao, Q. Gu, L. Zhao and W.-B. Luo, *Journal of Energy Storage*, 2023, **72**, 108740.
2. L. Wu, Y. Mei, Y. Liu, W. Xu, M. Zhang, Y. Dong and Z.-S. Wu, *Chemical Engineering Journal*, 2023, **459**, 141662.
3. S. Luo, J. Xu, B. Yuan, L. Chen, L. Xu, R. Zheng, Y. Wang, M. Zhang, Y. Lu and Y. Luo, *Carbon*, 2023, **214**, 118334.
4. Y. Zhang, Y. Liu, Z. Liu, X. Wu, Y. Wen, H. Chen, X. Ni, G. Liu, J. Huang and S. Peng, *Journal of Energy Chemistry*, 2022, **64**, 23-32.
5. M. H. Alfaruqi, J. Gim, S. Kim, J. Song, D. T. Pham, J. Jo, Z. Xiu, V. Mathew and J. Kim, *Electrochemistry Communications*, 2015, **60**, 121-125.
6. A. Dhiman and D. G. Ivey, *Batteries & Supercaps*, 2020, **3**, 293-305.
7. L. Chen, Z. Yang, H. Qin, X. Zeng and J. Meng, *Journal of power sources*, 2019, **425**, 162-169.
8. N. Liu, X. Wu, Y. Yin, A. Chen, C. Zhao, Z. Guo, L. Fan and N. Zhang, *ACS applied materials & interfaces*, 2020, **12**, 28199-28205.
9. D. Wang, L. Wang, G. Liang, H. Li, Z. Liu, Z. Tang, J. Liang and C. Zhi, *ACS nano*, 2019, **13**, 10643-10652.
10. F. Gao, B. Mei, X. Xu, J. Ren, D. Zhao, Z. Zhang, Z. Wang, Y. Wu, X. Liu and Y. Zhang, *Chemical Engineering Journal*, 2022, **448**, 137742.
11. J. Long, Z. Yang, F. Yang, J. Cuan and J. Wu, *Electrochimica Acta*, 2020, **344**,

136155.

12. J.-W. Xu, Q.-L. Gao, Y.-M. Xia, X.-S. Lin, W.-L. Liu, M.-M. Ren, F.-G. Kong, S.-J. Wang and C. Lin, *Journal of Colloid and Interface Science*, 2021, **598**, 419-429.

13. Y. Liu, X. Chi, Q. Han, Y. Du, J. Huang, Y. Liu and J. Yang, *Journal of Power Sources*, 2019, **443**, 227244.

14. S. Lian, C. Sun, W. Xu, W. Huo, Y. Luo, K. Zhao, G. Yao, W. Xu, Y. Zhang and Z. Li, *Nano Energy*, 2019, **62**, 79-84.